Catalysis Today 168 (2011) 96–111

Contents lists available at ScienceDirect

Catalysis Today

journal homepage: www.elsevier.com/locate/cattod

Hierarchical zeolites prepared by organosilane templating: A study of the synthesis mechanism and catalytic activity

Arjan J.J. Koekkoek[a], Christiaan H.L. Tempelman[a], Volkan Degirmenci[a], Meiling Guo[b], Zhaochi Feng[b], Can Li[b], Emiel J.M. Hensen[a,*]

[a] *Schuit Institute of Catalysis, Eindhoven University of Technology, P.O. Box 513, 5600 MB Eindhoven, The Netherlands*
[b] *State Key Laboratory of Catalysis, Dalian Institute of Chemical Physics, Chinese Academy of Sciences, 457 Zhongshan Road, Dalian 116023, China*

ARTICLE INFO

Article history:
Received 30 September 2010
Received in revised form 2 December 2010
Accepted 3 December 2010
Available online 8 January 2011

Keywords:
Hierarchical ZSM-5
Zeolite synthesis
Organosilane
Acid activity
Benzene oxidation

ABSTRACT

The crystallization of hierarchical ZSM-5 in the presence of the organosilane octadecyl-dimethyl-(3-trimethoxysilyl-propyl)-ammonium chloride as the mesoporogen was investigated as a function of time and temperature. The synthesis by this method proceeds in two steps. The rapid formation of a predominantly amorphous disordered mesoporous aluminosilicate precursor phase is followed by the formation of globular highly mesoporous zeolite particles involving dissolution of the precursor phase. It is difficult to completely convert the initial phase into the final hierarchical zeolite. This limits the amount of aluminium built into the MFI network and the resulting Brønsted acidity. In the presence of iron, more crystalline hierarchical zeolite is obtained. These Fe-containing zeolites are excellent catalysts for the selective oxidation of benzene to phenol. Their hierarchical pore structure leads to higher reaction rates due to increased mass transfer and increased catalyst longevity despite more substantial coke formation.

1. Introduction

Hierarchical zeolites and large pore silicates can overcome the pore size constraints and mass transfer limitations by decreasing diffusion path lengths [1–3]. Introducing substantial mesoporosity in zeolite crystals has become a very active research area in recent years. Among the novel approaches to arrive at mesoporous zeolites are carbon black scaffolding, polymer templating, desilication and agglomeration of nano-sized zeolites [3–7]. The unsuccessful initial attempts to combine templates for zeolite growth and the growth of ordered mesoporous silicas can be overcome by covalently linking mesoporogens to the growing zeolite crystal surface as shown by Choi et al. [8–10]. By using a trimethoxysilyl group in a mesoporogen such as cetyltrimethylammonium, Choi et al. [8] obtained highly mesoporous MFI type zeolite with improved catalytic activity. Recently, the benefit of this approach for the preparation of much improved [Fe]ZSM-5 catalysts for the selective oxidation of benzene to phenol by nitrous oxide was demonstrated [11]. The high connectivity between micropores and mesopores or, alternatively stated, the very small microporous domains in these hierarchical zeolites resulted in superior catalytic performance when compared to conventional microporous catalysts. Despite the ease of the organosilane templating method, the details of the synthesis mechanism and how the use of the organosilane template affects the catalytic properties remain to be addressed. Herein we report on our detailed investigations of the synthesis mechanism of HZSM-5 and [Fe]ZSM-5 templated by tetrapropylammonium bromide as the microporogen and octadecyl-dimethyl-(3-trimethoxysilyl-propyl)-ammonium chloride as the organosilane mesoporogen. We will follow the morphology, texture and catalytic properties of the materials as a function of the hydrothermal conditions (time and temperature). The acidic properties of the hierarchical HZSM-5 zeolites are investigated by Brønsted acid site titration and n-heptane hydroconversion. The catalytic performance of the Fe-containing zeolites will be compared by using nitrous oxide decomposition and selective oxidation of benzene to phenol.

2. Experimental

2.1. Synthesis of mesoZSM-5

MFI-type zeolites with substantial mesoporosity were synthesized using the hydrothermal procedure involving organosilanes as described by Choi et al. [8]. Zeolites were grown at different crystallization temperatures and times. In a typical procedure

---

[*] Corresponding author.
E-mail address: e.j.m.hensen@tue.nl (E.J.M. Hensen).

0920-5861/$ – see front matter © 2011 Elsevier B.V. All rights reserved.
doi:10.1016/j.cattod.2010.12.033

0.21 g sodium aluminate, 4.2 g tetrapropylammonium bromide and 1.2 g sodium hydroxide were dissolved in 202.5 ml of demineralized water. A second solution was made by mixing 12.9 g tetraethylorthosilicate (TEOS) with 2.07 g octadecyl-(3-trimethoxysilylpropyl)-ammonium chloride (TPOAC) in methanol (60% w/w). The silicate solution was added dropwise to the first solution yielding a synthesis gel with the molar composition $NaO/AlO_2/TPABr/TPOAC/Si/H_2O = 11/1/5.3/0.9/20/3750$. The gel was stirred at room temperature for 2 h and transferred to a Teflon lined stainless steel autoclave thereafter. The mixtures were hydrothermally treated in a static autoclave followed by rapid quenching. Products were recovered by filtration and washed with copious amounts of demi water and subsequently dried overnight at 100 °C. Organic templates were removed by calcination. Samples were heated in a flow of nitrogen (100 ml/min) at a heating rate of 1 °C/min to 550 °C, followed by exposure to artificial air at the same temperature for 4 h. Samples are denoted by mesoZSM-5(T, y) with T being the crystallization temperature and y the crystallization time in h. To convert the samples to the H^+ form they were ion exchanged three times with 1 M NH_4NO_3 for 8 h at 90 °C followed by calcination at 550 °C. A second set of samples was grown at 150 °C for 120 h at varying ratios of Si/TPOAC between 240 and 12. These samples are denoted by mesoZSM-5(T, 120, z) with z the ratio of Si/TPOAC. A reference sample denoted as TMS (TPOAC templated mesoporous silicate) was grown without TPABr by hydrothermal treatment at 125 °C for 24 h.

2.2. Synthesis of meso[Fe]ZSM-5

For the iron containing mesoporous Fe/ZSM-5 an adapted procedure described by Xin et al. was used [11]. Typically, 0.21 g sodium aluminate, 4.2 g of tetrapropylammonium bromide and 1.2 g sodium hydroxide were dissolved in 192.5 ml demineralized water. An iron precursor solution was made by dissolving 0.13 g of $Fe(NO_3)_3 \cdot 9H_2O$ in 10 ml demineralized water. A silicon precursor solution was made by mixing 12.9 g TEOS and 2.07 g TPOAC. Under vigorous stirring this solution was added dropwise to the first solution followed by the addition of the iron precursor solution. The resulting yellowish suspension was stirred at room temperature for 2 h and transferred to a Teflon lined stainless steel autoclave. Samples were hydrothermally treated in a static autoclave at 150 °C. The reaction was rapidly quenched and the samples were recovered by filtration and washed with copious amounts of demineralized water. Samples were dried overnight at 100 °C. The template was removed by Soxhlet extraction with methanol for 12 h followed by calcination. Samples were heated in a flow of nitrogen to 550 °C at a heating rate of 2 °C/min, followed by air calcination at 550 °C for 6 h. To convert the zeolites to the H^+ form they were three times ion exchanged with 1 M NH_4NO_3 at 90 °C for 8 h followed by calcination at 550 °C. Prior to the catalytic testing samples were steamed at 700 °C for 3 h in a flow of 10 vol% steam in nitrogen at a flow rate of 50 ml/min. Samples are denoted as meso[Fe]ZSM-5(150, y) with y the crystallization time in h.

2.3. Characterization

The metal content of the samples was analyzed by inductively coupled plasma optical emission spectroscopy (ICP-OES) on a Spectro CIROS CCD spectrometer equipped with a free-running 27.12 MHz generator at 1400 W. Prior to the measurement samples were dissolved in a mixture of $HF/HNO_3/H_2O$ (1:1:1).

UV–vis spectra were recorded on a Shimadzu UV-2401 PC spectrometer in diffuse-reflectance mode with a 60 mm integrating sphere. $BaSO_4$ was used as the reference. The spectra were transformed into the Kubelka–Munk function and subsequently deconvoluted into subbands by standard peak fitting software.

Infrared spectra were recorded on a Nicolet Avatar 360 spectrometer with a KBr pellet (1 mg of zeolite in 100 mg of KBr). IR crystallinities were determined by the ratio of the intensities of the band at 450 cm^{-1} and 550 cm^{-1} compared to a ZSM-5 reference standard [12,13].

XRD patterns were recorded on a Bruker D4 Endeavor powder diffraction system using Cu Kα radiation with a scanning speed of 0.0057° min^{-1} in the range of $0.5° \leq 2\theta \leq 5°$ and 0.01° min^{-1} in the range of $5° \leq 2\theta \leq 60°$. XRD crystallinities were determined using the Bruker TOPAS 3.0 software.

Nitrogen sorption isotherms were measured at −196 °C on a Micromeritics ASAP2020 system in static measurement mode. The samples were outgassed at 400 °C for 8 h prior to the sorption measurements. The Brunauer–Emmett–Teller (BET) equation was used to calculate the specific surface area (S_{BET}) from the adsorption data obtained ($p/p_0 = 0.05–0.25$). The mesopore volume (V_{meso}) and mesopore size distribution were calculated using the Barrett–Joyner–Halenda (BJH) method on the adsorption branch of the isotherm. The micropore area (S_{mic}) and micropore volume (V_{mic}) were calculated from the t-plot curve at thickness range between 3.5 and 5.4 Å [14,15]. The micropore size distribution was calculated using the Horvath–Kawazoe (HK) method for slit pore geometries applying Saito–Foley (SF) correction [16].

Transmission electron micrographs were obtained with a FEI Tecnai 20 instrument at an electron acceleration voltage of 200 kV. Typically, a small amount of sample was suspended in ethanol, sonicated and dispersed over a Cu grid with a holey carbon film.

Scanning electron microscopy (SEM) was performed using a Philips environmental scanning electron microscope FEIXL-30 ESEM FEG in high-vacuum mode at low voltage.

Magic angle spinning (MAS) ^{27}Al single pulse NMR spectra were recorded on a Bruker Avance DMX-500 NMR spectrometer equipped with a 2.5 MAS probe head operating at a magnetic field of 11.7 T (the Al resonance frequency at this field is 130.3 MHz). The ^{27}Al chemical shift is referred to a saturated $Al(NO_3)_3$ solution. In a typical experiment 10 mg of well-hydrated sample was packed in a 2.5 mm zirconia rotor. The MAS sample rotation speed was 25 kHz. The relaxation time was 1 s and the pulse length was 1 μs.

UV Raman spectra were recorded with a Jobin–Yvon triple stage spectrograph with spectral resolution of 2 cm^{-1}. The laser line at 244 nm of a Coherent Innova 300 Fred laser was used as exciting source with an output of 20 mW. The power of the laser on the samples was about 2 mW.

2.4. FTIR H/D exchange

H/D exchange of hydroxyl groups with perdeuterated benzene was followed in situ by infrared spectroscopy as described elsewhere [17]. Infrared spectra were recorded in transmission mode in a Bruker IFS-113v FTIR spectrometer with a mid-infrared DTGS detector. Typically, a powdered sample was pressed into a self-supporting wafer with a density $\rho = 10\ mg/cm^2$ and placed in an in situ cell. After calcining the catalyst wafer at 550 °C, the catalyst was evacuated to a pressure better than 2×10^{-6} mbar and temperature was lowered to 30 °C. A background spectrum was recorded. Perdeuterobenzene (C_6D_6, Merck, purity 99.96%) was introduced into the cell from a glass ampoule. The total volume of C_6D_6 administered to the cell was 0.33 mmol ±1%, resulting in a pressure of 10 mbar. IR spectra were recorded for different exposure times and temperatures. For each spectrum, 125 scans were accumulated at a resolution of 2 cm^{-1}. Difference spectra were obtained by subtracting the initial spectrum of the dehydrated sample from the spectra after exposure to C_6D_6.

Table 1
Textural properties and composition of the mesoZSM-5(*T*, *y*) catalyst grown as a function of the temperature and time of hydrothermal treatment.

Sample	C_{XRD}[a] (%)	C_{IR}[b] (%)	S_{BET} (m^2/g)	S_{mic} (m^2/g)	S_{meso} (m^2/g)	V_{mic} (cm^3/g)	V_{meso} (cm^3/g)	Si/Al	Al_{tetra} (%)	Al_{octa} (%)	N_{BAS}[c] (μmol/g)
MesoZSM-5(150, 0)	0	0	435	37	93	0.009	0.18	22	51	49	3
MesoZSM-5(150, 6)	25	69	684	70	555	0.034	0.41	33	69	31	9
MesoZSM-5(150, 24)	47	84	593	76	442	0.036	0.35	30	70	30	36
MesoZSM-5(150, 72)	61	85	569	117	387	0.060	0.30	28	74	26	51
MesoZSM-5(150, 120)	77	86	519	155	266	0.075	0.28	28	77	23	80
MesoZSM-5(150, 144)	87	87	486	174	198	0.083	0.25	31	77	23	96
MesoZSM-5(130, 6)	0	35	795	0	781	0	0.71	21	49	51	3
MesoZSM-5(130, 24)[d]	35	62	673	n.d.[e]	663	n.d.[e]	0.62	n.d.[e]	n.d.[e]	n.d.[e]	n.d.[e]
MesoZSM-5(130, 72)[d]	53	68	638	n.d.[e]	519	n.d.[e]	0.50	n.d.[e]	n.d.[e]	n.d.[e]	n.d.[e]
MesoZSM-5(130, 120)	59	71	619	20	446	0.012	0.51	24	73	27	50
MesoZSM-5(170, 6)	21	59	04	0	360	0	0.25	30	62	38	6
MesoZSM-5(170, 24)[d]	43	66	394	n.d.[e]	286	n.d.[e]	0.24	n.d.[e]	n.d.[e]	n.d.[e]	n.d.[e]
MesoZSM-5(170, 72)[d]	58	79	384	n.d.[e]	144	n.d.[e]	0.21	n.d.[e]	n.d.[e]	n.d.[e]	n.d.[e]
MesoZSM-5(170, 120)	80	80	388	231	90	0.110	0.11	33	80	20	71
HZSM-5	100	100	371	259	0	0.14	–	20	92	8	730
TMS[f]	0	0	921	0	702	0	0.48	32	n.d.[e]	n.d.[e]	4

[a] XRD crystallinity.
[b] IR crystallinity.
[c] Number of strong Brønsted acid sites.
[d] N_2 physisorption measured on Tristar 3000.
[e] Not determined.
[f] Mesoporous reference aluminosilicate sample grown with TPOAC as mesoporogen without TPABr.

2.5. Catalytic activity measurements

2.5.1. n-Heptane isomerisation

The concentration of strong Brønsted acid sites in the aluminosilicates was evaluated from catalytic activity measurements in the hydroconversion of n-heptane of Pd-loaded aluminosilicate [18–20]. To this end, a sieve fraction (250–500 μm) of aluminosilicate was loaded with 0.4 wt% Pd via incipient wetness impregnation with a solution of appropriate concentration of $Pd(NH_3)_4(NO_3)_2$. The resulting material was calcined at 300 °C. Prior to testing, the catalyst was reduced at 450 °C at 30 bar in flowing hydrogen (100 ml/min). Hydroconversion of n-heptane was carried out at 30 bar at a H_2/hydrocarbon ratio of 24 mol/mol. The reaction temperature was lowered from 450 to 200 °C at a rate of 0.2 °C/min.

2.5.2. Benzene oxidation with nitrous oxide

The amount of active Fe^{2+} centers on the meso[Fe]ZSM-5 series catalysts was determined by low temperature titration of the catalyst with N_2O. In a typical procedure 100 mg catalyst of a sieve fraction of 125–250 μm was placed in a quartz microreactor. The sample was heated in a flow of 20% O_2 in He (100 ml/min) to 550 °C and kept at this temperature for 4 h. Subsequently, the flow was switched to He and the sample was cooled to 250 °C. At this temperature the flow was switched to a mixture of 1.01% Ar, 0.98% N_2O in He and the evolution of N_2 was measured using a calibrated mass spectrometer. The amount of N_2 evolved was measured to determine the amount of active Fe^{2+} sites.

The activity of the catalysts for the decomposition of nitrous oxide was determined using a parallel plug flow quartz micro reactor. In a typical experiment 50 mg of sieved catalyst was placed in the quartz reactor tube and contained between two quartz wool plugs. The samples were calcined in artificial air by heating to 550 °C at a rate of 2 °C/min. After an isothermal period of 2 h, the catalysts were cooled to 250 °C. Subsequently, catalytic activity measurements were carried out in a flow of 5 vol% N_2O in He at a gas hourly space velocity of 24,000 ml h^{-1} g^{-1}. A well calibrated online mass spectrometer was used for quantification of the gaseous products.

The catalytic activity in the hydroxylation of benzene to phenol using nitrous oxide was determined in a microflow reactor system. Typically, 100 mg of catalyst of a sieve fraction 125–250 μm was placed in a quartz microreactor tube and calcined in artificial air by heating to 550 °C at a rate of 2 °C/min and maintaining this temperature for 2 h. After cooling the catalyst to 350 °C in the same mixture, the gas flow was switched to the reaction feed mixture. This mixture consisted of 1 vol% benzene and 4 vol% nitrous oxide in He (100 ml/min). The gas hour space velocity was 30,000 h^{-1}. The gas phase composition was determined by a combination of online gas chromatography (Hewlett-Packard GC-5890 equipped with an HP-5 column and a flame ionization detector) and mass spectrometer (Balzers TPG-215).

3. Results

3.1. Structural characterization

3.1.1. Influence of crystallization time

Table 1 collects the composition, the crystallinity and textural properties of the mesoZSM-5(150, *y*) series zeolites. All the hydrothermally treated samples have a Si–Al ratio around 30, which is slightly higher than in the initial synthesis gel. With increasing crystallization time the zeolite crystallinity increases. The IR crystallinity strongly increases during the first 24 h of crystallization and reaches its maximum at 87%. The IR crystallinity, obtained by the intensity ratio of the IR band at 550 cm^{-1} (characteristic for the double five ring motif of the MFI topology) and the 450 cm^{-1} band due to Si–O vibrations, relates to the local ordering of the aluminosilicate network. The XRD crystallinity increases much slower with the crystallization time. The maximum XRD crystallinity is similar to the maximum IR crystallinity but is only reached after 120 h of crystallization. The XRD crystallinity is developed in two stages. Initially, a rapid increase is observed during the first day followed by a more gradual increase.

The nitrogen physisorption isotherms and the PSD of these zeolites are shown in Fig. 1. The samples prepared at relatively short crystallization time show a type IV isotherm without a clear hysteresis loop, which is due to the small size of the mesopores. In time the isotherm changes towards a type I isotherm having a H4 hysteresis loop indicative of a material possessing both micro- and mesoporosity. The micropore volume of the mesoZSM-5(150, *y*) series increases with the extent of crystallization. Concomitantly, the mesopore volume and surface area show a gradual decrease. Whereas mesoZSM-5(150, 0) only has a very small micro-

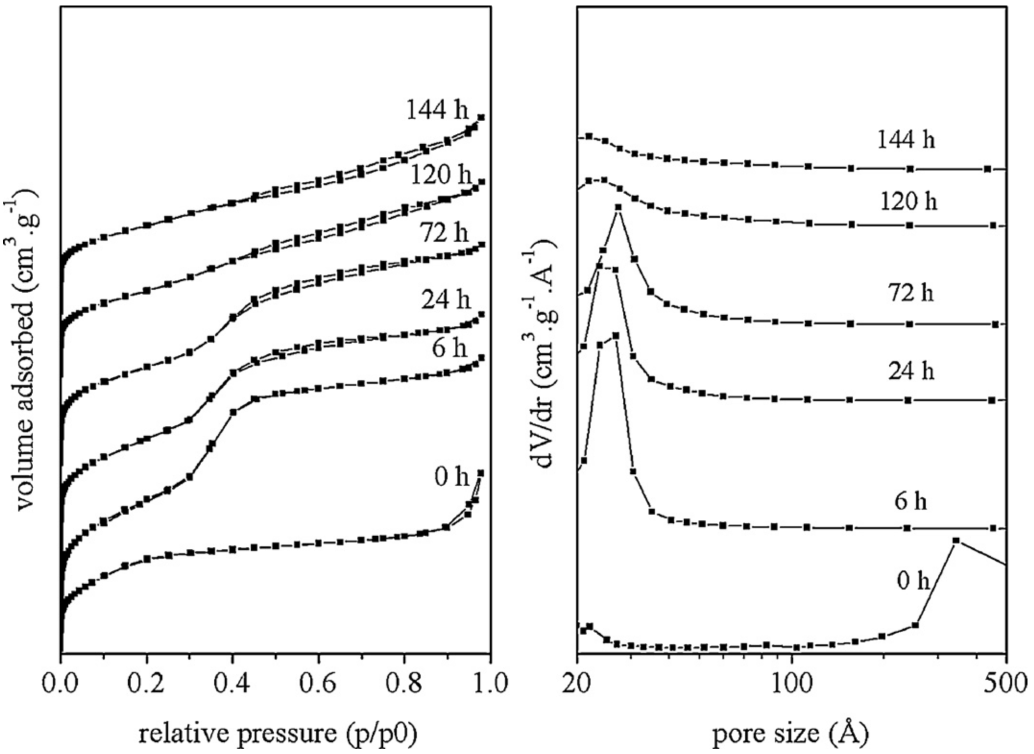

Fig. 1. Nitrogen physisorption isotherms (left) and BJH pore size distributions (right) for the mesoZSM-5(150, *y*) at different crystallization times.

pore volume and a disordered mesopore system, the material after 6 h crystallization has a relatively narrow mesopore size distribution around 2.5 nm. At the same time, substantial microporosity is developed in this material. Upon further crystallization this ordered mesophase becomes less pronounced with a gradual broadening of the mesopore size distribution and an increased contribution of micropores.

These latter changes are congruent to the changes in the XRD diffractograms (Fig. 2). Initially, only an amorphous disordered aluminosilicate phase is observed. The reflections at small angles for mesoZSM-5(150, 6) are characteristic for an ordered mesoporous silica. These distinct features erode with increasing crystallization time and are absent for the materials crystallized longer than 24 h. By including the XRD patterns of similar materials grown for 1, 2 and 3 h, it is clear that the order of the mesostructure increases up to 6 h after which it start to decrease again. In the corresponding wide angle XRD patterns the first features of the crystalline phase become already visible after 2 h crystallization.

Fig. 3 compares the UV Raman spectra excited at 244 nm of the calcined mesoZSM-5(150, *y*) series with spectrum of the ZSM-5 reference. The latter spectrum contains the characteristic MFI bands at 291, 379, 461 and 800 cm^{-1} [21]. The weaker bands in the high frequency region 1000–1200 cm^{-1} are typical of crystalline tetrahedral silica polymorphs [22]. The most intense Raman band at 379 cm^{-1} is assigned to the υ_s(Si–O–Si) mode belonging to five-membered rings of the MFI framework [23]. This band is sensitive to the degree of the crystallinity of the material [24]. The 379 cm^{-1} band is not observed in the mesoZSM-5 samples crystallized for 2 and 3 h. Conversely, it is very distinct in the materials crystallized for 6 h and longer. Although it is not possible to draw quantitative conclusions about the crystallinity, the evolution of the spectra indicates that the crystallinity of mesoZSM-5(150, 120) is considerably higher than that of the samples crystallized for 6 and 24 h. As the IR crystallinity of mesoZSM-5(120, 2) and mesoZSM-5(120, 3) was 25% and 42%, respectively, we conclude that the intensity of the band at 379 cm^{-1} correlates better with the long range ordering probed by XRD than with the short range ordering as determined by IR analysis.

Figs. 4 and 5 show representative transmission and scanning electron micrographs of the materials crystallized at 150 °C for various times. The sample isolated directly after hydrolysis of the starting chemicals contains aluminosilicate particles with sizes in the range of 10–100 nm. The morphology from SEM and TEM images is very similar to that of precipitated silica or silica–alumina [25]. Crystallization of the synthesis gel for 6 h results in a material with the typical wormhole pore structure reminiscent of mesoporous silicas such as KIT-1 [26]. This is expected, as the TPOAC template employed here is structurally similar to cetyltrimethylammoniumbromide (CTAB), which was shown to be an effective template for such disordered mesoporous aluminosilicates as KIT-1 by Zhao et al. [27]. MesoZSM-5(150, 6) contains only disordered mesoporous particles. The texture of mesoZSM-5(150, 72) is different. Next to the disordered mesoporous particles, large spherical particles are observed from the TEM micrographs. The scanning electron micrographs clearly show the presence of globular particles of several microns. The morphology of these particles is very similar to that reported for hierarchical zeolites grown by another organosilane template by Choi et al. [8]. In high resolution electron micrographs (Fig. 6) two further observations were made. Firstly, in some of the ordered mesoporous particles the onset of zeolite crystallization is observed by the presence of zeolite crystal planes. Such features are clearly observed in the sample crystallized for 24 h. Secondly, the large spherical particles appear to be made up from very small domains of crystalline material by inspection of their edges. With increasing crystallization time, the number of spherical particles grows at the expense of the ordered mesoporous silica phase. MesoZSM-5(150, 144) still contains a non-negligible amount of the amorphous mesoporous precursor phase.

Fig. 7 shows the ^{27}Al MAS NMR spectra of the mesoZSM-5(150, *y*) samples. All spectra are dominated by the strong signal around 57 ppm of tetrahedral aluminium. In addition all spectra show a weaker signal of octahedral aluminium at 0 ppm. The contribu-

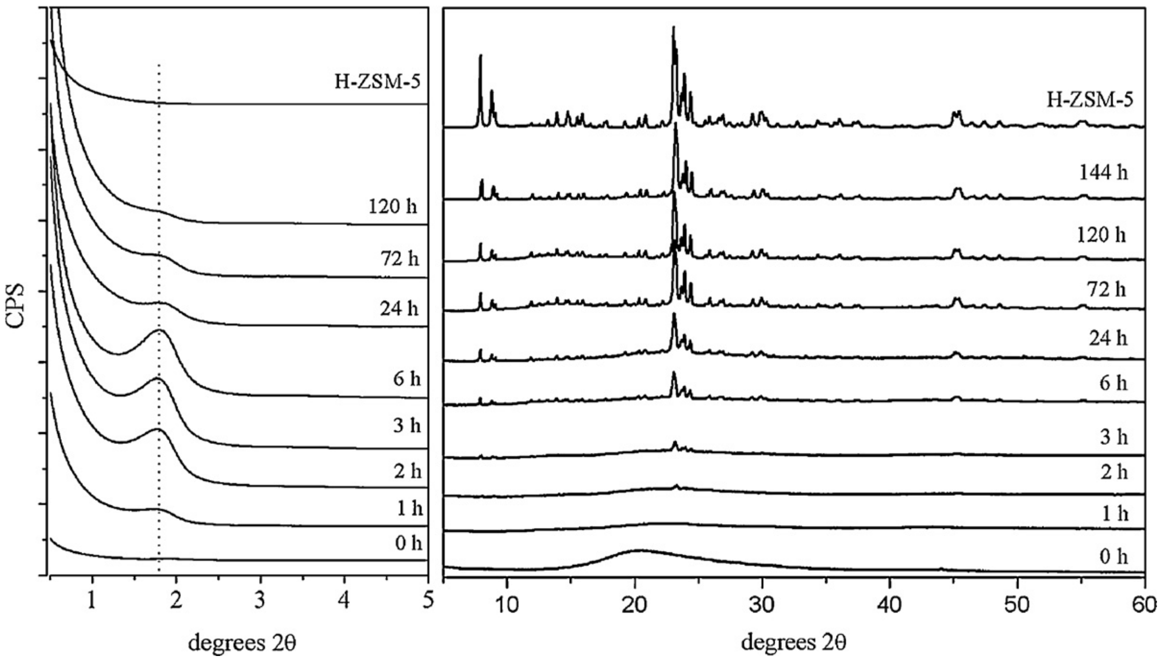

Fig. 2. Small angle (left) and wide angle (right) XRD diffractograms of the mesoZSM-5(150, y) series and the HZSM-5 reference zeolite.

tions of tetrahedral and octahedral Al nuclei are given in Table 1. Before crystallization an amorphous silica alumina gel is formed. Although a substantial part of Al is in tetrahedral coordination, this does not imply that Al is located in the silica network [25]. Instead, a substantial part of the Al is present on the surface of the silica particles observed in the electron micrographs in Fig. 3. The octahedral Al is either coordinated to the silica or has formed Al–O–Al linkages. Upon hydrothermal treatment for 6 h part of the aluminium changed its coordination to tetrahedral. This could be explained by the insertion of Al into the zeolite framework that is being formed. On the other hand, the surface area of the ordered mesoporous silica that has been formed is much higher than that of the phase obtained directly after precipitation. During this formation process, the redispersion of Al over the silica surface may take place.

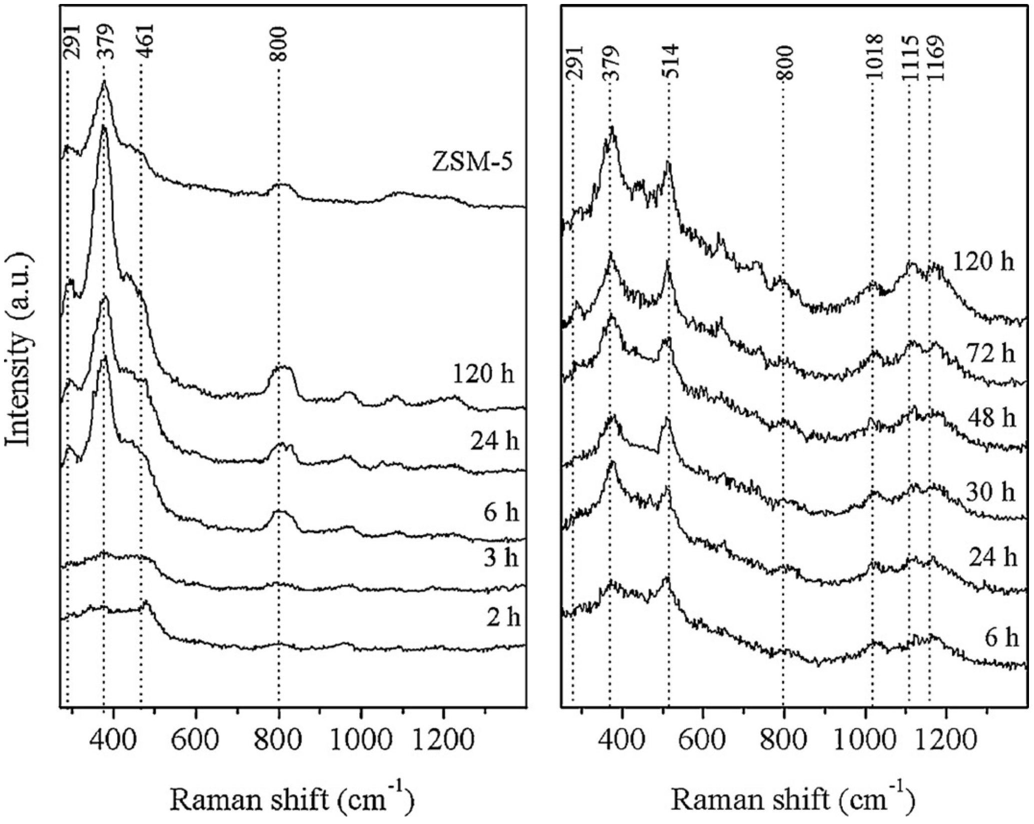

Fig. 3. Raman spectra (λ_{exc} = 244 nm) of mesoZSM-5(150, y) (left) and meso[Fe]ZSM-5(150, y) (right) samples at different crystallization times.

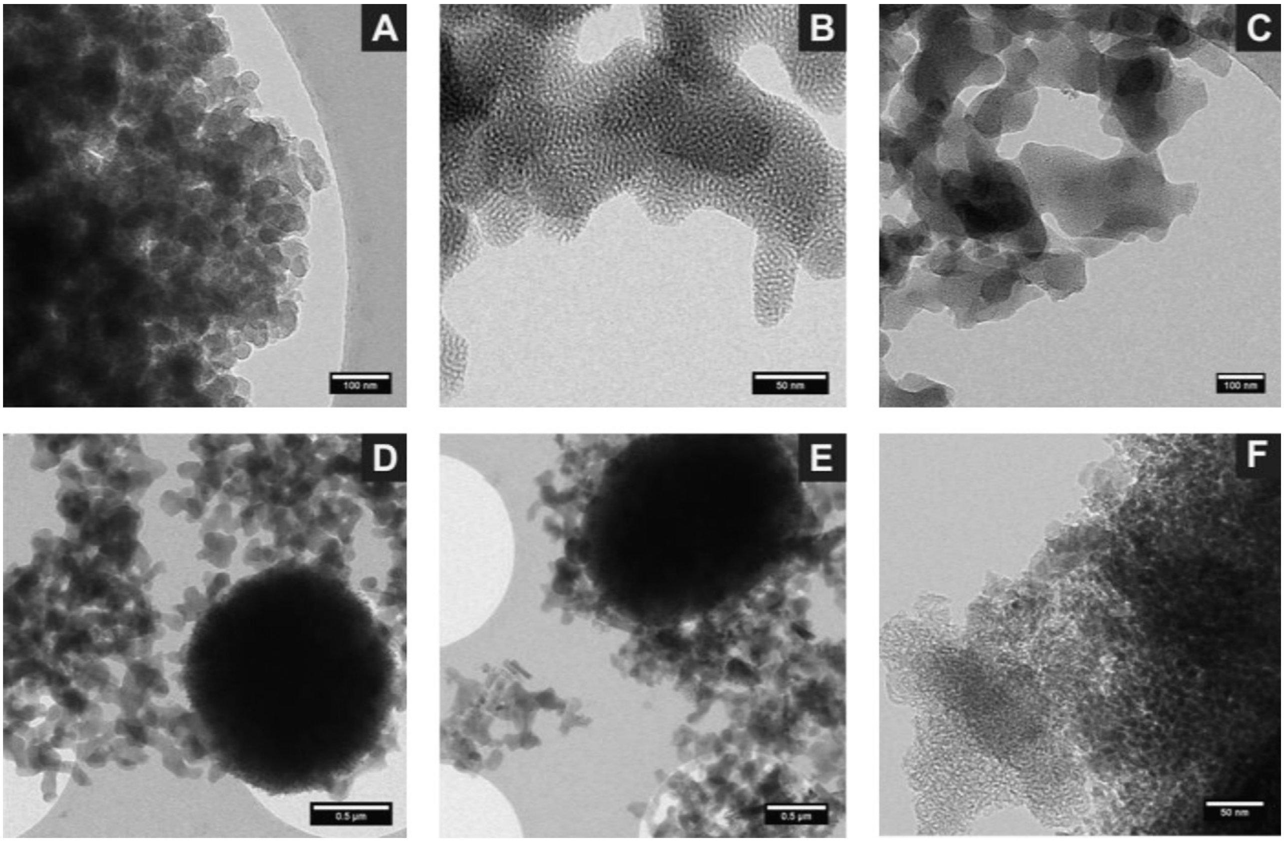

Fig. 4. TEM images of (a) mesoZSM-5(150, 0), (b) mesoZSM-5(150, 6), (c) mesoZSM-5(150, 24), (d) mesoZSM-5(150, 72), (e) mesoZSM-5(150, 120) and (f) mesoZSM-5(150, 144).

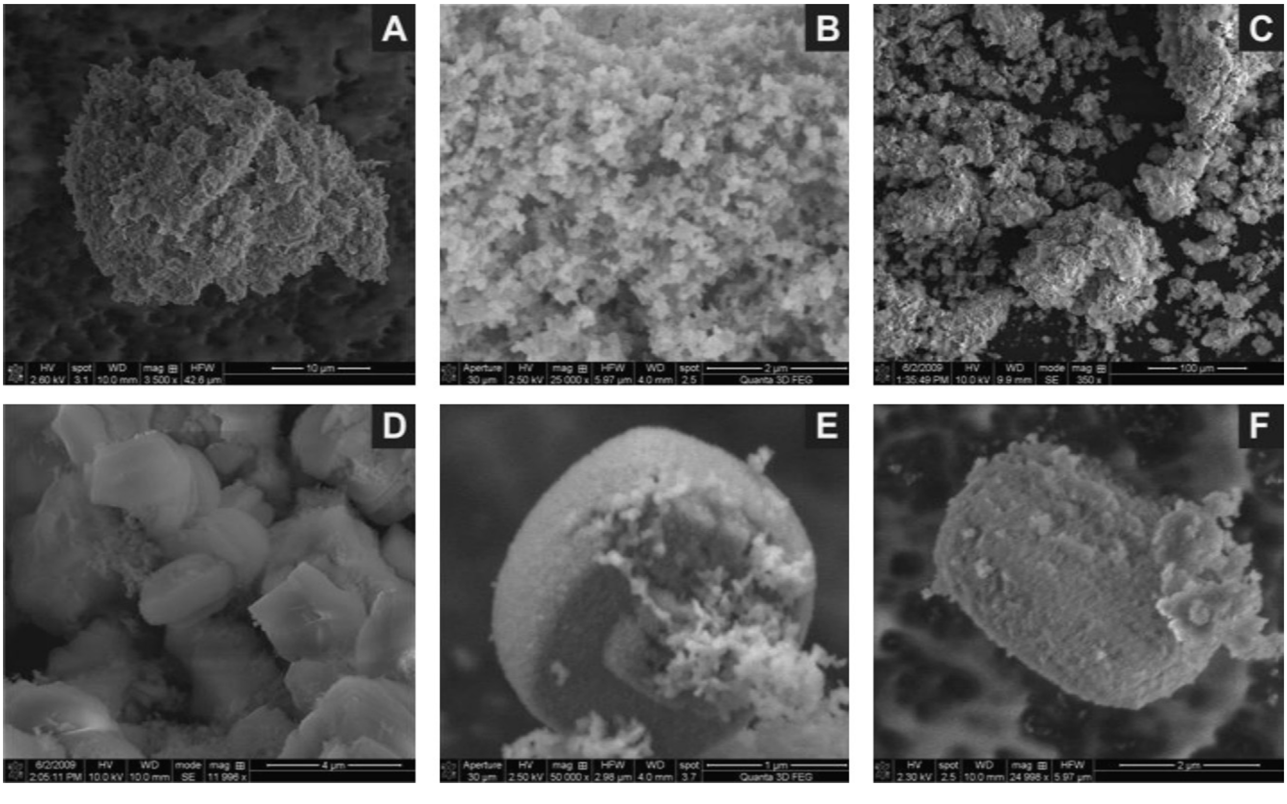

Fig. 5. SEM images of (a) mesoZSM-5(150, 0), (b) mesoZSM-5(150, 6), (c) mesoZSM-5(150, 24), (d) mesoZSM-5(150, 72), (e) mesoZSM-5(150, 120) and (f) mesoZSM-5(150, 144).

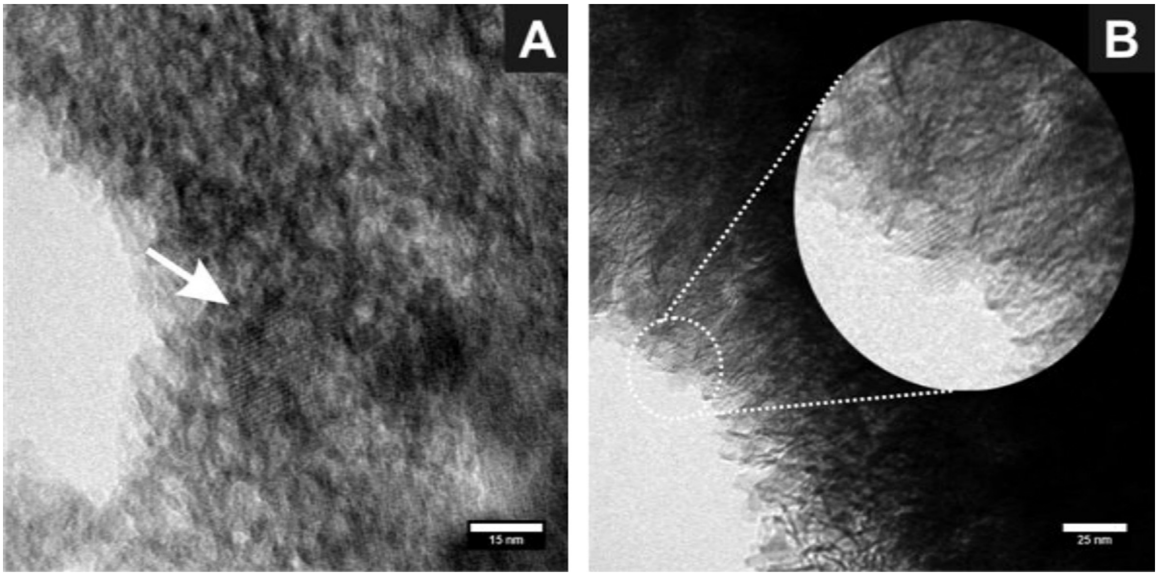

Fig. 6. High resolution TEM images of (a) crystalline planes in predominantly amorphous mesoZSM-5(150, 24) and (b) edge of a crystalline particle of mesoZSM-5(150, 120).

3.1.2. *Effect of the crystallization temperature*

The properties of the zeolite samples grown at 130 and 170 °C are given in Table 1. The samples grown at 170 °C have a similar Si/Al ratio of about 30 as the samples synthesized at 150 °C. The Si/Al ratio of the materials hydrothermally treated at 130 °C is much closer to the initial gel Si/Al ratio. As these samples have a much lower crystallinity than those synthesized at higher temperatures, it may be suggested that the Al is lost during the crystallization process. The trends in crystallinity for comparative samples prepared at 130, 150 and 170 °C as a function of the hydrothermal synthesis time are very similar. The IR crystallinity of samples synthesized at 130 °C is somewhat lower than of those synthesized at higher temperatures. The XRD crystallinity is much lower for these samples. For all samples the IR crystallinity increases with crystallization time. Similar to mesoZSM-5(150, *y*) IR crystallinities increase rapidly during the initial stage of the hydrothermal treatment and reach a maximum after 24 h. Noteworthy is that hydrothermal treatment at 150 °C gives the highest IR crystallinity, whereas a temperature of 170 °C is usually considered as the optimum temperature for ZSM-5 growth. For all temperatures the XRD crystallinity increases much slower. Crystallization at 170 °C gives comparable XRD crystallinities to hydrothermal treatment at 150 °C.

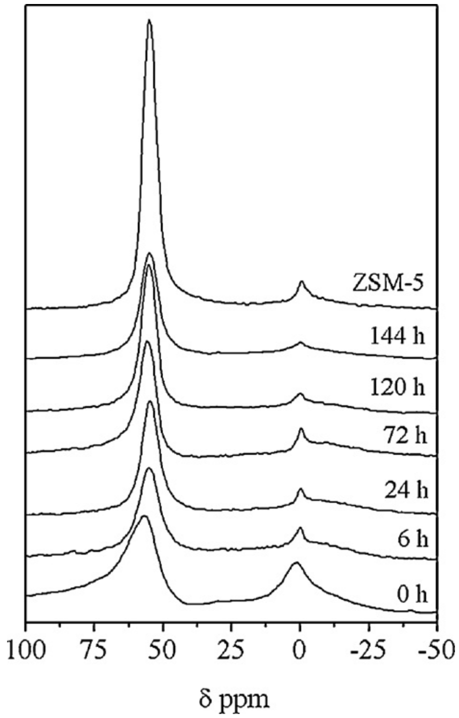

Fig. 7. Normalized ^{27}Al MAS spectra of the mesoZSM-5(150, *y*) samples and the HZSM-5 reference zeolite.

Nitrogen physisorption isotherms and corresponding BJH pore size distributions of the samples crystallized at different temperatures are shown in Fig. 8. For comparison the sample crystallized at 150 °C is included. MesoZSM-5(130, 6) and mesoZSM-5(170, 6) have mesopores but no or few micropores. The mesopore volume decreases with the crystallization temperature. All three mesoZSM-5(*T*, 6) samples show a relatively narrow PSD centered in the range 2–3 nm. Increasing the crystallization time to 120 h leads to large differences between the samples. The shape of the isotherm of mesoZSM-5(130, 120) is very similar to that of mesoZSM-5(130, 6) and the presence of mesopores with a size of about 2.5 nm is still clear. The isotherm of mesoZSM-5(150, 120) has changed substantially as compared to that of mesoZSM-5(150, 6). The sharp uptake around p/p_0 0.35 is absent and, instead, a gradual uptake occurs over the p/p_0 range above 0.5 in combination with a type IV hysteresis loop. This behavior is typical for mesoporous materials lacking order on the mesopore scale which is reflected by the broad peak in the BJH pore size distribution. The isotherm of mesoZSM-5(170, 120) has a more pronounced type I shape typical of a microporous material. The weak type IV hysteresis loop indicates limited mesoporosity.

The XRD patterns are depicted in Fig. 9. The small angle region shows a broad reflection for all materials crystallized for 6 h indicative of the ordered mesoporosity. The order increases with increasing crystallization temperature. Crystallization for 120 h leads to the nearly complete loss of the low angle reflection. The wide angle part of the diffractograms shows that only distinct reflections of the MFI structure are observed after 6 h crystallization for mesoZSM-5(150, 6) and mesoZSM-5(170, 6). After 120 h, also mesoZSM-5(130, 120) shows these reflections, albeit that they are much weaker than in the corresponding samples crystallized at higher temperatures.

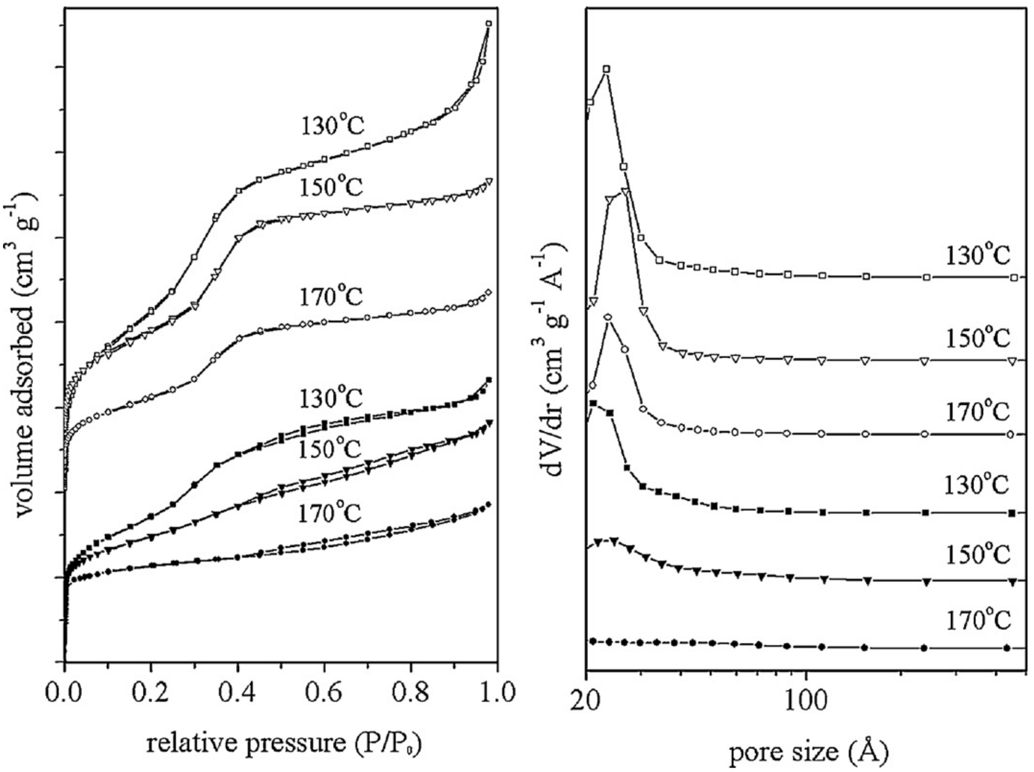

Fig. 8. Nitrogen physisorption isotherms (left) and BJH pore size distributions (right) for mesoZSM-5 samples crystallized for 6 (dotted lines) and 120 h (solid lines) at various temperatures.

Fig. 10 shows representative transmission and scanning electron micrograph images of samples grown at 130 and 170 °C. The morphologies of mesoZSM-5(130, 6) and mesoZSM-5(170, 6) have the similar wormhole mesopore structure as the sample crystallized at 150 °C. After 120 h crystallization, the electron micrographs show substantial differences in morphology and texture. MesoZSM-5(130, 120) predominantly contains particles without the initial wormhole mesoporous structure. Some zeolite crystal particles are observed in the micrographs. MesoZSM-5(170, 120) appears as a physical mixture of large zeolite crystals and small elongated fragments of what is crystalline material. High resolution electron microscopy confirms the presence of microporous domains of 50–100 nm size.

The contributions of tetrahedral and octahedral Al in these zeolites are given in Table 1. The differences in the Al distribution between the mesoZSM-5(*T*, 120) samples is very small, albeit that

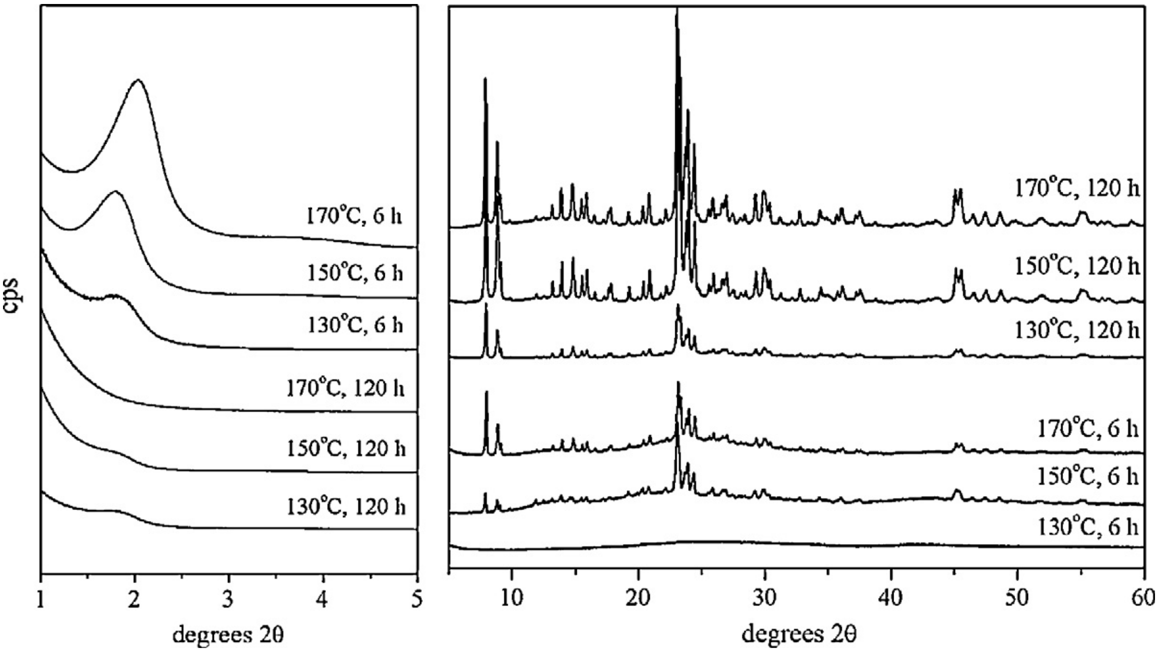

Fig. 9. Small angle (left) and wide angle (right) XRD diffractograms of the mesoZSM-5 samples grown at different temperatures.

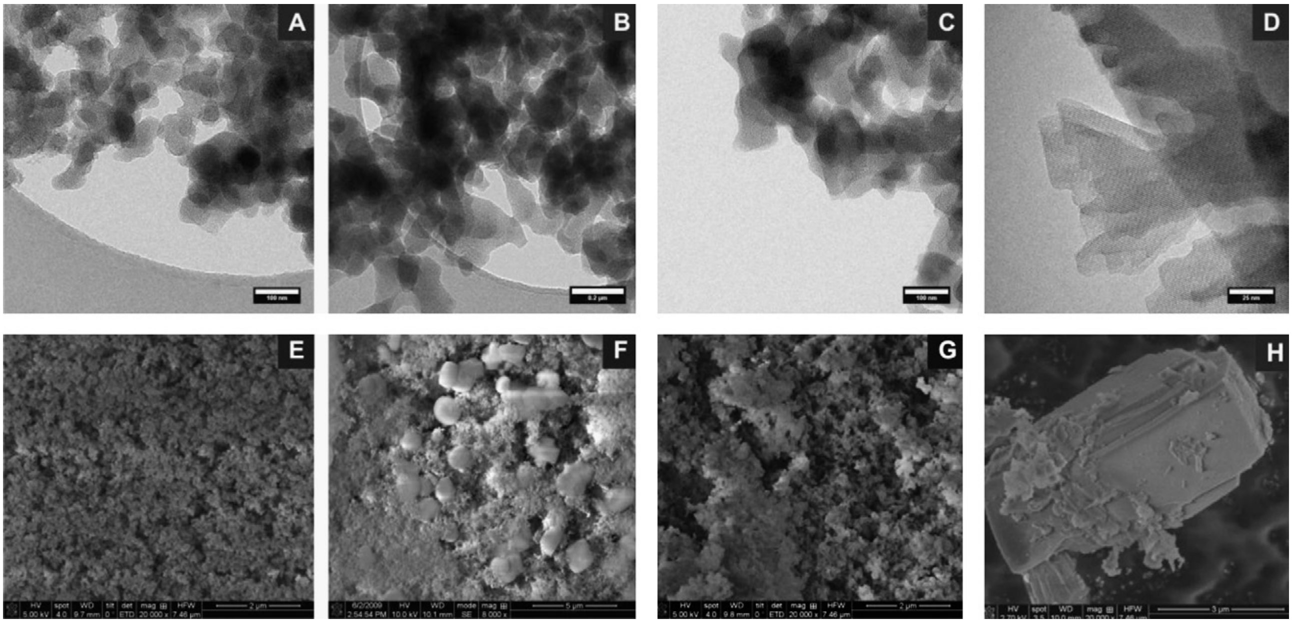

Fig. 10. Representative TEM pictures of (a) mesoZSM-5(130, 6), (b) mesoZSM-5(130, 120), (c) meso-ZSM-5(170, 6), (d) meso-ZSM-5(170, 120) and SEM pictures of (e) mesoZSM-5(130, 6), (f) meso-ZSM-5(130, 120), (g) mesoZSM-5(170, 6) and (h) mesoZSM-5(170, 120).

the tetrahedral contribution increases somewhat with the crystallization temperature.

3.1.3. Influence of the organosilane template content

To explore the influence of the organosilane template amount a series of zeolites was grown at increasing Si/TPOAC ratios. To this end, the TPOAC amount was varied in the synthesis gel, while keeping the amounts of all other ingredients constant. Table 2 collects the physical and morphological properties of the materials synthesized at Si/TPOAC ratios at a temperature of 150 °C and a crystallization time of 120 h. Figs. 11–13 contain the nitrogen physisorption isotherms and BJH PSDs, XRD patterns and electron micrographs, respectively. The crystallinity strongly depends on the amount of TPOAC used in the synthesis. When the amount of TPOAC is doubled compared to the reference sample, an amorphous aluminosilicate is obtained as evidenced by the absence of XRD reflections at high angles. The nitrogen physisorption isotherm is of the type IV type with a H1 hysteresis loop confirming that a mesoporous silica is formed. The surface area of this material is about 900 m^2/g and the PSD indicates the presence of pores in the range of 2–3 nm. This agrees with the strong low angle reflection around 1.9° and the TEM images, which show the wormhole pore structure as observed before. With decreasing amount of TPOAC, zeolite crystallinity appears as determined by XRD and IR analysis. In parallel, the hysteresis loop changes from H1 to H4 representative of hierarchical pore systems with disordered mesopores. In agreement with this, the distinct presence of well-defined mesopores in mesoZSM-5(150, 120, 12) has disappeared. TEM images of these samples show that the morphology is that of a well integrated mixture of mesoporous silica with crystalline domains. The surface area and pore volume decreases with decreasing Si/TPOAC ratio. At the lowest Si/TPOAC ratio, the crystallinity has increased to 95%. The isotherm has a pronounced type I shape indicative of a microporous system. Note that the Si/Al ratios are all around 30.

3.1.4. Meso[Fe]ZSM-5

The XRD patterns of these meso[Fe]ZSM-5 materials (not shown) show a very similar trend to those of the mesoZSM-5(150, *y*) series. A low angle reflection present at relatively short crystallization times disappears with increasing crystallization, showing that the initial mesoscale order is lost. Also the nitrogen physisorption data (Table 3) are similar to the mesoZSM-5(150, *y*) series. Initially, the sample crystallized for 6 h shows a type IV isotherm with a sharp uptake in the region p/p_0 0.35–0.4 which is reflected by the narrow BJH pore size distribution centered around 3 nm. Already this sample shows a substantial amount of microporosity. Increasing the crystallization time leads to a gradual increase in microporosity at the expense of the mesoporosity. The isotherm shows a type I character with a gradual uptake over the whole range p/p_0 0.4–0.9 indicative of the disordered mesopore system which is consistent with the interpretation of the XRD data.

Representative SEM images of several meso[Fe]ZSM-5(*y*) catalysts are depicted in Fig. 14. The sample crystallized for 6 h shows only an amorphous phase. After 24 h the morphology of the sample is quite different. Besides the amorphous phase several large globular ZSM-5 shaped mesoporous particles have formed. After 72 h of crystallization the electron micrographs are completely dominated by the highly mesoporous ZSM-5 particles. Besides the fact that for these meso[Fe]ZSM-5 samples the particles form much faster

Table 2
Textural properties and composition of the mesoZSM-5(*T*, *y*) catalysts.

Catalyst	Si/TPOAC	C_{XRD} (%)	C_{IR} (%)	S_{BET} (m^2/g)	S_{mic} (m^2/g)	S_{meso} (m^2/g)	V_{mic} (cm^3/g)	V_{meso} (cm^3/g)	Si/Al	N_{BAS}[a] (μmol/g)
MesoZSM-5(*T*, 12)	12	0	20	871	73	801	0.021	0.99	28	3
MesoZSM-5(*T*, 24)	24	77	86	519	155	266	0.075	0.30	33	n.d.[b]
MesoZSM-5(*T*, 48)	48	86	88	556	170	270	0.076	0.41	31	n.d.[b]
MesoZSM-5(*T*, 240)	240	96	95	450	224	214	0.101	0.20	29	93

[a] Number of strong Brønsted acid sites.
[b] Not determined.

Table 3
Textural properties and composition of the meso[Fe]ZSM-5(T, y) catalysts.

Catalyst	C_{XRD} (%)	C_{IR} (%)	S_{BET} (m^2/g)	S_{mic} (m^2/g)	S_{meso} (m^2/g)	V_{mic} (cm^3/g)	V_{meso} (cm^3/g)	Si/Al	Si/Fe	Fe^{2+} ($\mu mol/g_{cat}$)
Meso[Fe]ZSM-5(150, 6)	40	47	618	38	565	0.018	0.40	36	105	7
Meso[Fe]ZSM-5(150, 24)	57	61	584	173	393	0.069	0.32	34	111	6
Meso[Fe]ZSM-5(150, 30)	56	82	525	195	319	0.076	0.30	31	115	33
Meso[Fe]ZSM-5(150, 48)	85	98	504	195	315	0.079	0.31	30	119	51
Meso[Fe]ZSM-5(150, 72)	87	99	492	189	306	0.083	0.33	33	104	n.d.[a]
Meso[Fe]ZSM-5(150, 120)	91	99	495	192	303	0.082	0.32	36	109	52
[Fe]ZSM-5	>99	>99	356	218	138	0.12	0.10	46	97	77

[a] Not determined.

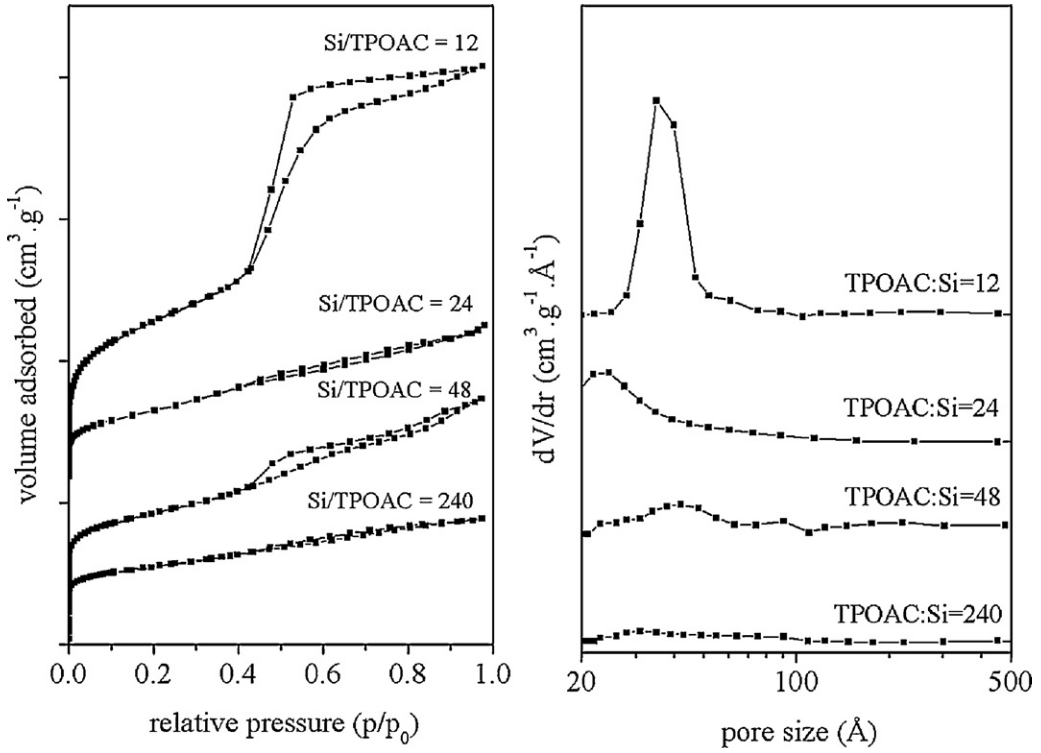

Fig. 11. Nitrogen physisorption isotherms (left) and BJH pore size distributions (right) of the mesoZSM-5(T, y) series crystallized as a function of the Si/TPOAC ratio.

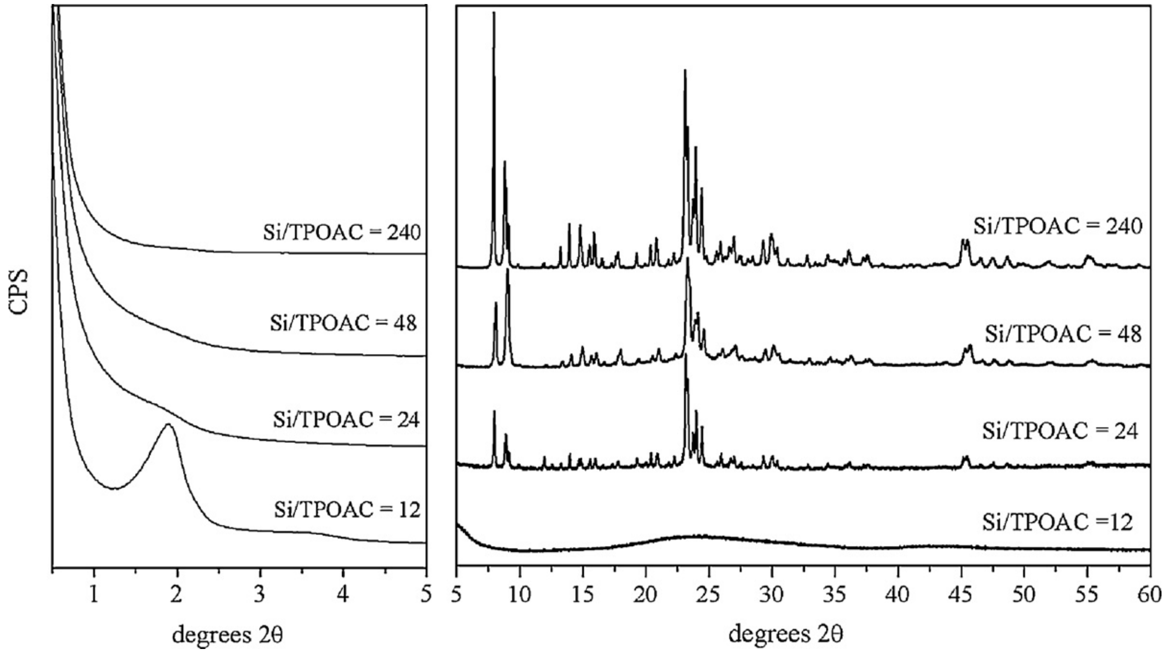

Fig. 12. Small angle (left) and wide angle (right) powder XRD patterns of the mesoZSM-5(T, y) samples grown at 150 °C with different Si/TPOAC ratios.

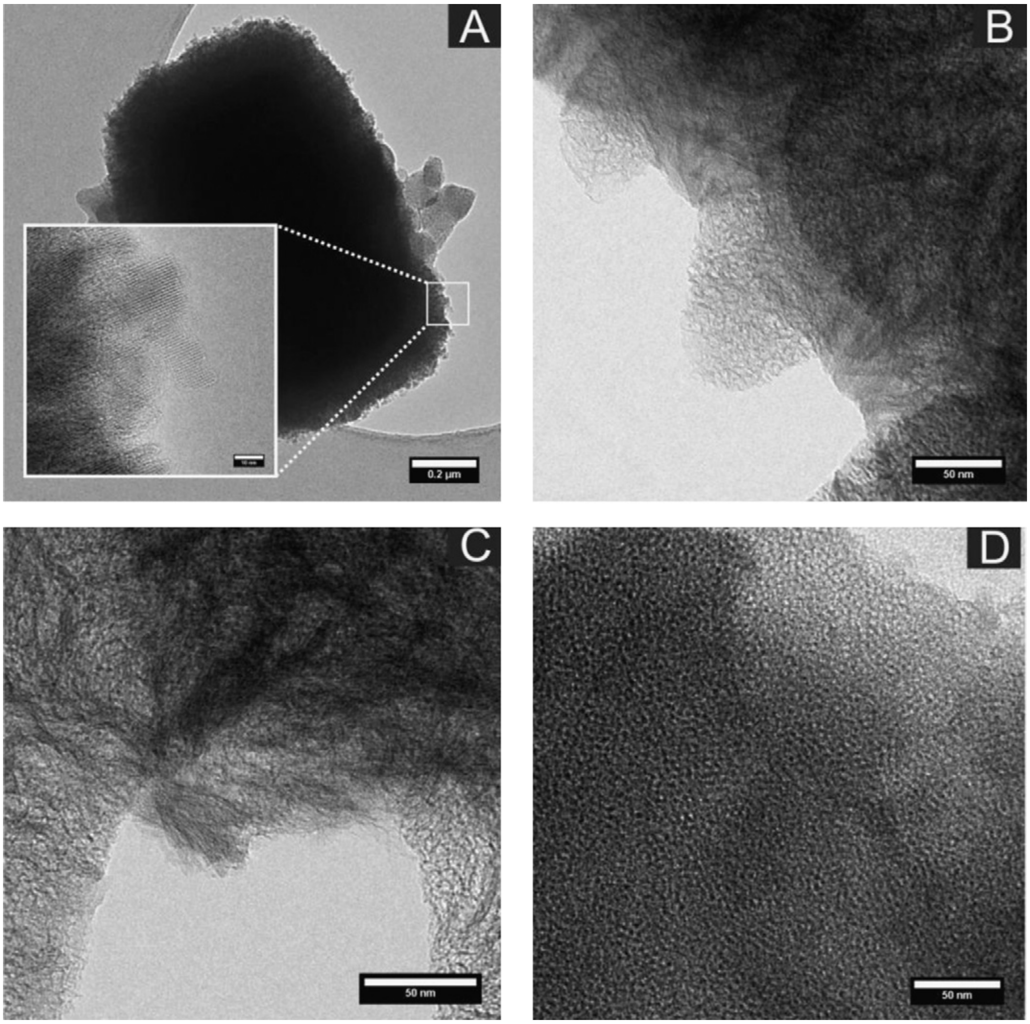

Fig. 13. Representative TEM images of (a) mesoZSM-5(*T*, 240), (b) mesoZSM-5(*T*, 48), (c) mesoZSM-5(*T*, 24) and (d) mesoZSM-5(*T*, 12).

compared to the mesoZSM-5 series, the particles exhibit a different shape as well. The meso[Fe]ZSM-5 samples show a dish-like structure with clear subunits on the flat sides of the dish, which is sometimes observed for ZSM-5 crystals [28,29].

The iron speciation in these materials was studied by DR-UV–vis and UV-Raman spectroscopy. Fig. 15 shows the UV–vis spectra of the as-synthesized catalysts. The spectrum of the material obtained before any hydrothermal treatment shows several absorption bands in the visible region indicating the presence of a large number of different iron species. The strong absorption in the UV region is caused by the TPOAC which has a strong adsorption in this region. After 6 h hydrothermal treatment the spectrum has changed completely. The spectrum is now dominated by the intense oxygen to metal charge transfer bands of isolated iron silicate species consisting of tetrahedral coordinated iron in framework positions (245 nm) and octahedral iron complexes (277 nm) [30–32]. Upon further hydrothermal treatment the spectra do not show any significant changes. Especially, the absence of absorption bands at higher wavelengths shows that large iron oxide aggregates are absent. Upon calcination the spectra show an additional absorption band around 333 nm caused by small oligomeric iron oxide clusters [33,34]. The relative differences between the spectra of the calcined materials are very small suggesting the iron coordination in the catalysts does not change significantly with the extent of crystallization. Specifically, the amount of clustered iron oxides in this set of samples is very small.

The UV-Raman spectra of these materials at various crystallization stages are given in Fig. 3b. The intensities of the relevant bands in these spectra are lower than those for the mesoZSM-5 series. The difference is caused by minute amounts of the organic template molecules that cause fluorescence radiation and suppresses the intensities of the interesting bands. Fan et al. have used a template-free synthesis to study the formation mechanism of Fe/ZSM-5 [33]. The band corresponding to the crystalline ZSM-5 framework at 379 cm^{-1} is clearly visible for crystallization times above 6 h. In meso[Fe]ZSM-5(150, 6) this band is a bit weaker than in the other spectra, in agreement with its somewhat lower crystallinity. In meso[Fe]ZSM-5(150, 24) this band and the one at 800 cm^{-1} can be observed, indicating the formation of the crystalline MFI framework. Another characteristic band of the MFI structure at 291 cm^{-1} is only clearly observed in the spectra of the samples crystallized for 30 h and more. The use of an excitation laser at 244 nm results in resonance enhancement of the bands whose absorption energy falls in the range of the p–d transitions of [Fe]ZSM-5. Thus, besides the characteristic bands of ZSM-5 four additional bands at 514, 1018, 1115, and 1169 cm^{-1} are observed in the spectra of the meso[Fe]ZSM-5 series and most clearly so in the spectrum of meso[Fe]ZSM-5(150, 120). These bands are related to the ZSM-5 framework iron species [33–35]. The bands at 514 and 1115 cm^{-1} are the symmetric and asymmetric stretching vibrational modes of the ZSM-5 framework Fe–O–Si species. The band at 1018 cm^{-1} is due to Si–O–Si bonds in proximity of framework Fe species. The

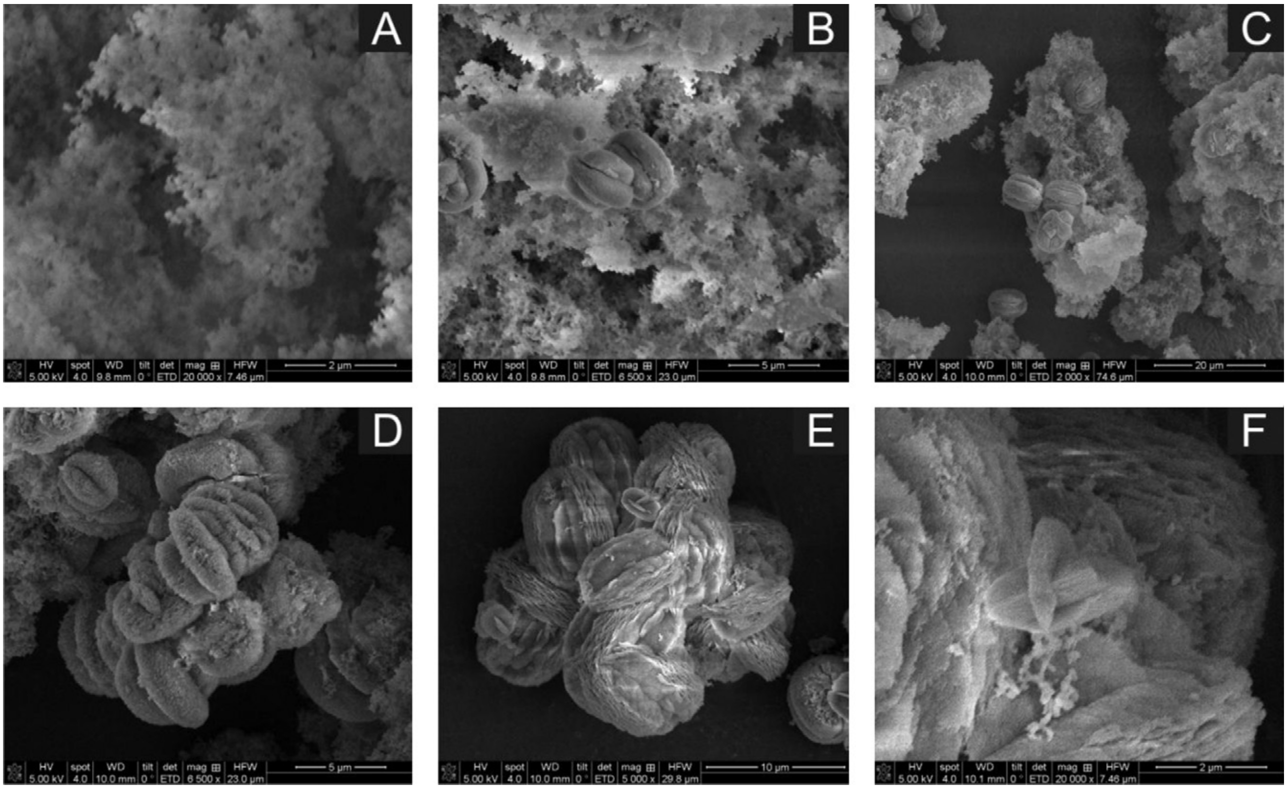

Fig. 14. Representative SEM images of the meso[Fe]ZSM-5 zeolites grown for (a) 6 h, (b) 24 h, (c) 30 h, (d) 72 h and (e and f) 120 h.

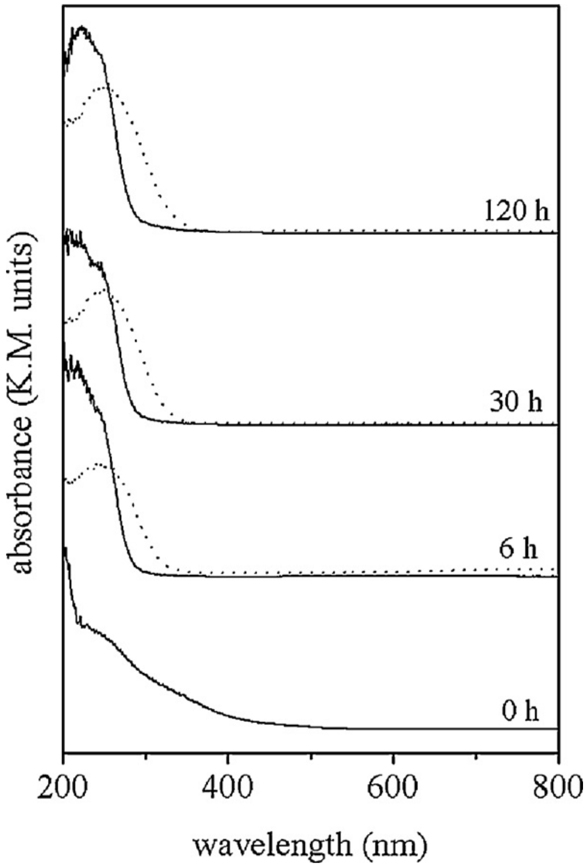

Fig. 15. Diffuse-reflectance UV–vis spectra of the meso[Fe]ZSM-5(150, 120, *y*) samples for different crystallization times, before (solid) and after (dotted) calcination.

band at 514 cm^{-1} becomes sharper with increasing zeolite crystallization. Whereas the bands at 1115 and 1169 cm^{-1} are only observed as a broad band in meso[Fe]ZSM-5(150, 6), further crystallization makes the bands sharper and distinguishable as two separate bands. At relatively low crystallinity the iron atoms are not coordinated as rigid as in the fully crystalline samples, which explains the broad band between 1100 and 1200 cm^{-1}. However, with prolonged crystallization more iron atoms are incorporated into the ZSM-5 crystalline phase in tetrahedral framework positions.

3.2. *Acidity characterization of mesoZSM-5*

The number of strong Brønsted acid sites (BAS) in the mesoZSM-5 series was determined by selective H/D exchange FT-IR spectroscopy [17,20]. This method is based on the exchange of the strongly acidic hydroxyl groups by deuterium by exposure to perdeuterobenzene. This method is particularly useful for samples containing a small amount of BAS next to a larger number of weakly and non-acidic silanol groups as typically found in (partially) amorphous aluminosilicates.

Table 1 collects the BAS densities for the mesoZSM-5 series. The acid site density of the HZSM-5 reference sample of 730 μmol/g is very close to the content of tetrahedral Al (750 μmol/g) as determined from its Al content (Si/Al = 20) and ^{27}Al NMR spectrum (92% Al^{IV}). MesoZSM-5(150, 0) and mesoZSM-5(150, 6) contain less than 10 μmol/g BAS. Such acid site densities are typical for amorphous silica–aluminas [25]. The former sample is amorphous in nature and thus can be best described as an amorphous silica–alumina. Despite the higher crystallinity of mesoZSM-5(150, 6) the number of strong BAS is still very small. Only upon further crystallization does the BAS density increase. The correlation of the BAS density with the XRD crystallinity is stronger than with the IR crystallinity. The highest BAS density of the mesoZSM-5 series crys-

Table 4
n-Heptane hydroconversion activities expressed as temperature required for 40% conversion for several mesoZSM-5 and reference catalysts.

Catalyst	$T_{40\%}$ (°C)
MesoZSM-5(130, 0)	350
MesoZSM-5(150, 0)	353
MesoZSM-5(150, 6)	350
MesoZSM-5(150, 72)	267
MesoZSM-5(150, 120)	255
MesoZSM-5(170, 6)	350
MesoZSM-5(170, 120)	252
HZSM-5	221
TMS[a]	355
ASA[b]	357

[a] Reference sample prepared without TPOAC.

[b] Amorphous silica–alumina with a nominal Al_2O_3 content of 5 wt% [20].

tallized at 150 °C is 96 μmol/g for mesoZSM-5(150, 144). This is considerably lower than the amount of tetrahedral Al in this sample (370 μmol/g) and implies that a substantial part of the Al has not been built into the crystalline zeolite framework. Crystallization at 130 °C results in lower BAS densities, while the acidities of the materials crystallized at 170 °C are quite similar to the values determined for the materials synthesized at 150 °C.

To verify these trends, the catalytic activity in the hydroconversion of n-heptane was determined for a subset of these catalysts. This bifunctional reaction involves dehydrogenation and hydrogenation of alkanes and alkenes by a metal function (Pd) and isomerisation and cracking of the intermediate olefins. The Pd content is chosen such that the rate is determined by the acid catalyzed reaction of olefins. There is general agreement that strong Brønsted acidity is required for the isomerisation and cracking reactions [18–20]. As an indication of the acid activity, the temperature to obtain a conversion of n-heptane of 40% is chosen. The results summarized in Table 4 clearly show that mesoZSM-5(150, 0) and mesoZSM-5(150, 6) have very low activities in alkane hydroconversion. The activity is in the same range as that of amorphous silica–aluminas [25]. Crystallization for 72 and 120 h results in zeolites with T_{40} values of 267 and 255 °C. These activities are still considerably lower than that of HZSM-5 (T_{40} = 221 °C) in line with the difference in acid site density. The activities of zeolites synthesized at 130 and 170 °C are also in line with the trends for the BAS densities.

3.3. Catalytic activity of meso[Fe]ZSM-5

The number of active Fe^{2+} species for the Fe/ZSM-5 catalysts was determined by titration with nitrous oxide at 250 °C [36,37]. At this temperature N_2O decomposes stoichiometrically to molecular nitrogen and a surface oxygen atom that has been linked to the oxidation of benzene. Table 3 summarizes the active Fe^{2+} densities. Although UV–vis spectroscopy does not show significant changes in the iron speciation between the samples, the Fe^{2+} active site density strongly increases with the extent of crystallization. After 6 h the number of active sites is only 7 μmol/g_{cat}. This number is significantly higher after 24 h crystallization and reaches a maximum of 51 μmol/g_{cat} after 48 h hydrothermal treatment. The number of active sites in these highly crystalline catalysts hydrothermally treated for several days is approximately 30% lower than in the conventional microporous Fe/ZSM-5 catalyst.

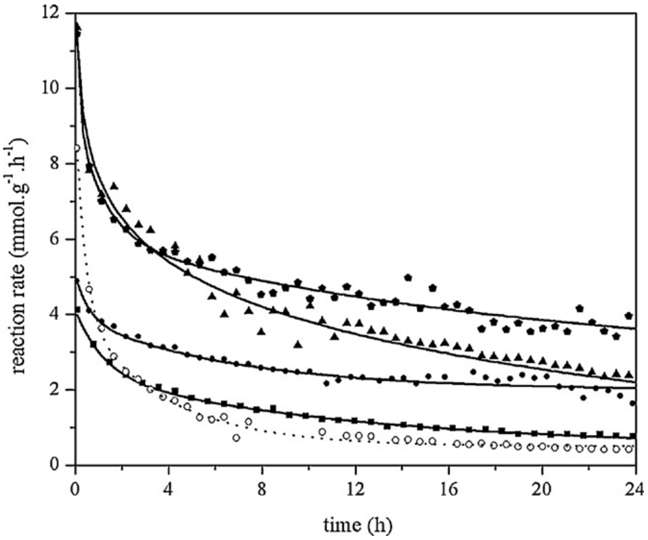

Fig. 16. Rate of phenol formation for meso[Fe]ZSM-5 catalysts crystallized for (■) 6 h, (●) 24 h, (▲) 30 h and (⬟) 120 h (solid lines) and (○) [Fe]ZSM-5 (dotted line).

The catalytic activity of the meso[Fe]ZSM-5 series was determined in the catalytic decomposition of nitrous oxide and the oxidation of benzene with nitrous oxide. Table 5 lists the temperature required for a N_2O conversion of 50% ($T_{50\%}$) in nitrous oxide decomposition. Clearly, the catalytic activity strongly increases with the crystallization time. Consequently, there also appears to be a strong correlation between the activity and the amount of Fe^{2+} sites. The activity of meso[Fe]ZSM-5(150, 120) is very close to that of the reference Fe/ZSM-5 zeolite. The activities of these samples are very close to those reported earlier for hydrothermally synthesized FeZSM-5 zeolites [31]. On the other hand, the activities of zeolites with a higher Fe content prepared for instance by chemical vapor deposition of $FeCl_3$ [24] are considerably higher. The reason is that hydrothermally prepared Fe/ZSM-5 zeolites contain more isolated Fe sites from which recombinative oxygen desorption is more difficult than from iron oxide clusters.

Fig. 16 shows the rate of phenol formation of the meso[Fe]ZSM-5 catalysts. Activity data are summarized in Table 5. Meso[Fe]ZSM-5(150, 6) shows the lowest initial activity, as expected from its small number of active sites. Increasing the crystallization time to 24 h results in a small increase of the initial activity. The catalyst longevity of both meso[Fe]ZSM-5(150, 6) and meso[Fe]ZSM-5(150, 24) is much higher than of the reference [Fe]ZSM-5 catalyst. As a result of this improved catalyst lifetime, the total TON after 24 h of reaction of meso[Fe]ZSM-5 is larger than that of the reference [Fe]ZSM-5. Meso[Fe]ZSM-5(150, 30) shows a much higher initial

Table 5
Benzene oxidation and N_2O decomposition data for the meso[Fe]ZSM-5(T, y) and [Fe]ZSM-5 reference catalysts.

Catalyst	Benzene oxidation				N_2O decomposition
	$R_{initial}$ (mmol/g_{cat} h)	R_{int} (h^{-1})	TON (g_{ph}/g_{cat})	C (mg/g_{cat})	$T_{50\%}$ (°C)
Meso[Fe]ZSM-5(150, 6)	3.99	570	33	49	596
Meso[Fe]ZSM-5(150, 24)	4.87	811	61	48	585
Meso[Fe]ZSM-5(150, 30)	11.31	343	95	57	524
Meso[Fe]ZSM-5(150, 48)	11.01	217	107	93	520
Meso[Fe]ZSM-5(150, 120)	11.46	220	114	115	504
[Fe]ZSM-5	8.34	108	26	76	497

activity compared to meso[Fe]ZSM-5(150, 24) in line with the higher amount of Fe^{2+} species. A further increase of the hydrothermal treatment does not have a significant effect on the initial activity. The TON on the other hand increases with crystallization time. As a result meso[Fe]ZSM-5(150, 120) shows a phenol production which is four times larger compared to the reference [Fe]ZSM-5 in line with our earlier finding [11]. As carbonaceous by-product are the main cause for catalyst deactivation [30,38,39], the amount of coke deposits was determined after 24 h reaction time by temperature programmed oxidation. Table 5 shows that meso[Fe]ZSM-5(150, 6) contains the lowest amount of coke deposits. With increasing productivity the amount of carbonaceous products increases.

4. General discussion

Crystallization of a typical synthesis gel of ZSM-5 zeolite at 150 °C in the presence of an organosilane such as octadecyl-(3-trimethoxysilylpropyl)-ammonium chloride results in the formation of ZSM-5 zeolites with a hierarchical pore structure. Texturally, these zeolites are made up from very small microporous zeolite domains with sizes below 50 nm integrated into highly mesoporous particles. The synthesis involves the initial partial pre-organization of the silicate oligomers followed by the formation of a largely amorphous disordered mesoporous aluminosilicate phase and subsequent crystallization of the final micron-sized highly mesoporous zeolite particles. Precipitation of the synthesis gel at room temperature results in a completely amorphous silica–alumina mixture without any atomic ordering of the aluminosilica phase. The textural properties of this material are very similar to those of amorphous silica–aluminas prepared by precipitation and related methods [25]. Hydrothermal synthesis at 130 °C and higher temperatures for 6 h results in a disordered mesoporous aluminosilica phase with a much higher mesopore surface area than the amorphous precursor material. This is the result of the templating action of TPOAC. A synthesis involving only TPOAC as the template gave a material with very similar textural properties. A substantial difference on the local scale is due to the presence of TPA ions in the mesoZSM-5 synthesis. These organic cations drive the formation of ZSM-5 zeolite. Hydrothermal treatment results in the formation of local domains with some resemblance to the zeolite MFI structure. The short range ordering of the aluminosilica phase into very small domains with characteristics of MFI zeolite can be followed by vibrational spectroscopy (IR and Raman), while the long range ordering can be probed by XRD analysis. In line with current insights into zeolite synthesis [40], hydrothermal synthesis at 130 °C is sufficient to pre-organize the silica oligomers into MFI fragments. The local ordering strongly increases with the crystallization time and temperature. Clearly, the assembly of precursor building units into larger domains that can be considered zeolitic as probed by XRD analysis proceeds at a much slower rate. The final crystallinity of the organosilane-modified zeolites is lower than that of conventional HZSM-5. The electron micrographs evidence the presence of two phases. Initially, a disordered mesoporous aluminosilica phase is rapidly formed. A substantial part of this phase exhibits short range structural features of MFI zeolite. The formation of a second phase starts after about 6 h crystallization at 150 °C. This phase consists of globular particles consisting of very small zeolite domains arranged in a highly accessible mesoporous matrix. Texture analysis shows that during the formation of these globular particles the micropore volume increases at the expense of the mesopore volume. Inspection of many electron micrographs suggests that, although the crystallization of the zeolite phase commences in the amorphous phase, the main growth mechanism involves dissolution of the initially formed mesoporous aluminosilica phase and growth of the globular particles (Ostwald ripening) [41]. Because the mesoporosity of the intermediate amorphous mesoporous and the final crystalline phases are due to the TPOAC mesoporogen, it is likely that the TPOA molecules initially present in the amorphous phase are also built into the globular particles through a dissolution process. This process thus involves the rehydrolysis of the TPOA–O–Si fragments. In agreement with this, we found that the use of calcined TMS as the Si source for the TPABr templated zeolite synthesis only resulted in microporous ZSM-5 without mesoporosity. In other words, the presence of the TPOAC template is essential during the formation of the final mesoporous zeolites. This mechanism provides a reasonable explanation for the relatively slow increase of the long range compared to short range order. Another implication is that the formation of an intermediate disordered mesoporous silica phase appears to be a non-essential artefact of this particular synthesis method.

When the hydrothermal treatment is carried out at lower temperature (130 °C), the crystallization is slower and the initial disordered mesophase dominates after prolonged synthesis time. On the other hand, hydrothermal synthesis at 170 °C results in a higher micropore volume at the expense of the mesopore volume. Larger zeolite domains are noted in the electron micrographs, which is tentatively explained by the instability of the Si–C bonds in the mesoporogen [42], resulting in its expulsion from the growing zeolite phase. Also in the latter case full crystallization into MFI zeolite cannot be obtained.

At a Si/TPOAC ratio of 24 the final crystallinity is limited to about 87%. Such a sample contains some amorphous material consisting of the disordered mesoporous aluminosilica phase. The final crystallinity can be improved by lowering the TPOAC content in the synthesis gel. This results in a decrease (increase) of the final mesopore (micropore) volume. Noteworthy is also that a too high TPOAC content prevents completely zeolite growth. From this it may be inferred that a too low Si/TPOAC ratio stabilizes nearly all silicate species in the amorphous disordered mesophase. The hydrophobicity of the TPOA stabilized particles probably prevents their hydrolysis. At a Si/TPOAC ratio of 240 a nearly fully crystalline mesoporous ZSM-5 zeolite is obtained with favorable textural properties.

The presence of Fe^{3+} in the synthesis gel also appears to accelerate the crystallization process. The final crystallinity is also higher. This finding contrasts earlier reports about the negative effect of Fe^{3+} on the crystallization of MFI zeolites [43]. A major difference with conventional MFI synthesis is the requirement of dissolution of the initially formed disordered mesoporous silica phase. The textural properties of the disordered mesophase in meso[Fe]ZSM-5(150, 6) is very similar to those in mesoZSM-5(150, 6). Thus, it may be that Fe^{3+} aids in the dissolution process.

An important area of application of zeolites is in the field of acid catalysis. Zeolite acidity resides in sites involving tetrahedral aluminium cations in substitution position for silicon in the framework. It is not straightforward to determine the number of such acid sites in aluminosilicates, especially in the presence of non-crystalline material. The present results show that the initially formed amorphous disordered aluminosilicate has only a very small number of acid sites, comparable to that of amorphous silica–aluminas [25]. This agrees with the nearly complete absence of atomic ordering. The high content of tetrahedral Al can be understood in terms of Al atoms grafted to the silica surface. Precipitation of silica at high pH in the presence of Al mainly affords isolated and clustered Al species on the silica surface [25]. The acidity strongly increases with the XRD crystallinity as evidenced by the increase in the number of strong Brønsted acid sites and the activity in n-heptane hydroconversion. This stresses the necessity of sufficient framework rigidity for the development of strong Brønsted acidity.

Despite its relatively high crystallinity the number of strong BAS in mesoZSM-5(150, 144) is about four times lower than the amount of tetrahedral Al as probed by ^{27}Al NMR. This suggests that the amount of Al atoms built into the zeolite particles is limited and a considerable fraction remains in the amorphous aluminosilica phases. This supposition is confirmed by EDX analysis of the globular crystalline and amorphous particles in mesoZSM-5(150, 144). The Si/Al ratio of the former is around 20, while the amorphous remains have a Si/Al ratio close to 10. Where the increase in the Si/TPOAC to 240 proved to be beneficial for obtaining high crystallinity, there is only a small increase in the number of strong Brønsted acid sites. Thus, the synthesis of hierarchical zeolites with TPOAC as carried out here is not conducive to the formation of highly acidic zeolites.

Whereas for acid catalyzed hydroisomerisation there is a need for strong Brønsted acid sites in zeolites the active sites for benzene oxidation are quite different. All Fe-containing catalysts show much improved performance with respect to the amount of phenol produced during 24 h time on stream when compared to the reference [Fe]ZSM-5. This improved performance is due to the highly mesoporous nature of the zeolite crystals. The initial activity (R_{initial}) strongly depends on the extent of crystallization of the ZSM-5 framework. The higher the crystallinity, the higher the density of active Fe^{2+} sites and the reaction rate of phenol. Although the crystallinity of meso[Fe]ZSM-5(150, 6) is much lower than that of [Fe]ZSM-5 resulting in a lower initial activity of the hierarchical zeolite, the deactivation of the former is much less pronounced leading to a higher production of phenol after 24 h time on stream. The beneficial textural properties affect the catalytic performance in two ways. First, the initial activity of all hierarchical meso[Fe]ZSM-5 zeolites is much higher than that of the reference zeolite. The intrinsic initial activities (R_{int}) normalized per active Fe^{2+} site gives a value of 811 $\text{mol}_{\text{phenol}}/\text{mol}_{Fe^{2+}}$ h for meso[Fe]ZSM-5(150, 24). The intrinsic activity decreases with increasing degree of crystallization and the active site content. A reasonable explanation is the increasing mass transport resistance due to the increasing size of the zeolite domains. Indeed, the XRD crystallinity increases and the mesopore surface area decreases going from meso[Fe]ZSM-5(150, 24) to meso[Fe]ZSM-5(150, 120). Moreover, the decrease in the intrinsic reaction rate is strongest between the two samples that show a strong increase in the XRD crystallinity (meso[Fe]ZSM-5(150, 24) and meso[Fe]ZSM-5(150, 30)). The maximum overall activity is already reached after 30 h of crystallization, implying that there is an optimum between active site density (high XRD crystallinity) and the size of the zeolite domains (high mesoporosity). Secondly, deactivation by carbonaceous deposits becomes less pronounced for the hierarchical zeolites. The long diffusion path of the phenol product in the pores of microporous [Fe]ZSM-5 result in the formation of by-products of high molecular weight [38]. Thus, clogging of the micropores renders a large part of the micropore space of this catalyst inaccessible, which explains the strong deactivation as a function of the time on stream. The microporous domains are much smaller in the hierarchical zeolites. Another way to state this is that the external surface area of the microporous part of these zeolites is much higher. This does not only lead to increased mass transport rates of reactants and products but also to a higher effectiveness factor of the micropore space. The deactivation due to active site inaccessibility to reactants in the microporous domains will become smaller with decreasing size of the microporous zeolite domains. On the other hand, we cannot exclude that part of the oxidation reaction takes place in the mesopores, that is, on the external walls of the microporous zeolite domains. We have earlier shown that this is in principle possible [44]. As a result of these effects, the catalyst longevity of the hierarchical zeolite is much improved. The reaction rate after 24 h time on stream of meso[Fe]ZSM-5(150, 120) is still much higher than that of [Fe]ZSM-5 underpinning the high accessibility of the hierarchical zeolite particles. Despite the almost four times higher TON the total amount of carbonaceous products formed in meso[Fe]ZSM-5(150, 120) is only 30% higher than in [Fe]ZSM-5. This suggests the intrinsic higher selectivity of the reaction in the hierarchical zeolite and can be explained by smaller residence times in the microporous reaction zone which will lead to an increased selectivity for reactions of the type benzene → phenol → carbonaceous products.

5. Conclusions

The growth of the mesoporous ZSM-5 using an amphiphilic organosilane as the mesopore structure directing agent proceeds in two steps. Firstly, an amorphous mesoporous aluminosilica phase is rapidly formed, followed by recrystallization into highly mesoporous zeolite crystals. The zeolite domain size is very small in these hierarchical zeolites. The recrystallization process involves the dissolution of the initial phase and growth of the final globular zeolite crystals. Complete consumption of the initial amorphous phase is not possible under conditions leading to highly mesoporous zeolites. As a result, a large part of the aluminium remains in the amorphous phase and the Brønsted acidity of the resulting material is low compared to conventional HZSM-5 zeolite at a similar Si/Al ratio. In the second step this phase acts as a nutrient for the growth of the hierarchical zeolite. The lower acidity of these hierarchical zeolites is a result low amount of aluminium incorporated in the crystalline phase, likely due to initial formation of a stable amorphous aluminosilicate phase. Addition of iron to the synthesis gives enhanced crystallization rates yielding hierarchical Fe/ZSM-5 which shows higher crystallinity as compared to the hierarchical ZSM-5. In the acid catalyzed hydroisomerisation the mesoporous ZSM-5 catalysts show an increasing activity with increasing crystallization time. The lower activity of these mesoZSM-5 materials is a direct result of the low amount of aluminium incorporated. For the selective oxidation of benzene the meso[Fe]ZSM-5 catalysts show an increasing initial activity and an increasing turnover number with increasing crystallization time.

Acknowledgements

This research was funded by the Netherlands Organization for Scientific Research. The authors acknowledge the Royal Netherlands Academy of Arts and Science and the Chinese Ministry of Science and Technology for financial support for travel and the Soft Matter Cryo-TEM Research Unit of the Eindhoven University of Technology for access to the TEM facility. E.H. and V.D. thank the Technology Foundation STW for financial support.

References

[1] A. Corma, Chem. Rev. 97 (1997) 2373–2420.
[2] S. van Donk, A.H. Janssen, J.H. Bitter, K.P. de Jong, Catal. Rev. 45 (2003) 297–319.
[3] J. Pérez-Ramírez, C.H. Christensen, K. Egeblad, C.H. Christensen, J.C. Groen, Chem. Soc. Rev. 37 (2008) 2530–2542.
[4] F.S. Xiao, Top. Catal. 35 (2005) 9–24.
[5] J.C. Groen, J.A. Moulijn, J. Perez-Ramirez, J. Mater. Chem. 16 (2006) 2121–2131.
[6] K. Egeblad, C.H. Christensen, M. Kustova, C.H. Christensen, Chem. Mater. 20 (2008) 946–960.
[7] D.P. Serrano, J. Aguado, J.M. Escola, J.M. Rodriguez, A. Pera, J. Mater. Chem. 18 (2008) 4210–4218.
[8] M. Choi, H.S. Cho, R. Srivastava, C. Venkatesan, D.H. Choi, R. Ryoo, Nat. Mat. 5 (2006) 718–723.
[9] H. Wang, T.J. Pinnavaia, Angew. Chem. Int. Ed. 45 (2006) 7603–7606.
[10] F.S. Xiao, L.F. Wang, C.Y. Yin, K.F. Lin, Y. Di, J.X. Li, R.R. Xu, D.S. Su, R. Schlögl, T. Yokoi, T. Tatsumi, Angew. Chem. Int. Ed. 45 (2006) 3090–3093.
[11] H.C. Xin, A.J.J. Koekkoek, Q. Yang, R.A. van Santen, C. Li, E.J.M. Hensen, Chem. Commun. (2009) 7590–7592.
[12] J.C. Jansen, F.J. van der Gaag, H. Bekkum, Zeolites 4 (1984) 369–372.
[13] D.B. Shukla, V.P. Pandya, J. Chem. Tech. Biotechnol. 44 (1989) 147–154.
[14] B.C. Lippens, J.H. de Boer, J. Catal. 4 (1965) 319–323.
[15] M. Kruk, M. Jaroniec, A. Sayari, Stud. Surf. Sci. Catal. 129 (2000) 587–596.
[16] A. Saito, H.C. Foley, AIChE J. 37 (2004) 429–436.

[17] D.G. Poduval, J.A.R. van Veen, M.S. Rigutto, E.J.M. Hensen, Chem. Commun. 46 (2010) 3466–3468.

[18] G.E. Gianetto, G.R. Perot, M.R. Guisnet, Ind. Eng. Chem. Prod. Res. Dev. 25 (1986) 481–490.

[19] J.W. Thybaut, C.S. Laxmi Narasimhan, J.F. Denayer, G.V. Baron, P.A. Jacobs, J.A. Martens, G.B. Marin, Ind. Eng. Chem. Res. 44 (2005) 5159–5169.

[20] E.J.M. Hensen, D.G. Poduval, D.A.J.M. Ligthart, J.A.R. van Veen, M.S. Rigutto, J. Phys. Chem. C 114 (2010) 8363–8374.

[21] P.K. Dutta, M. Puri, J. Phys. Chem. 91 (1987) 4329–4333.

[22] P. McMillan, Am. Mineral. 69 (1984) 622–644.

[23] K. Dutta, M. Puri, J. Phys. Chem. 91 (1987) 4329–4333;
P.K. Dutta, K.M. Rao, J.Y. Park, J. Phys. Chem. 95 (1991) 6654–6656.

[24] S. Mintova, B. Mihailova, V. Valtchev, L. Konstantinov, J. Chem. Soc. Chem. Commun. 15 (1994) 1791–1792.

[25] E.J.M. Hensen, D.G. Poduval, P.C.M.M. Magusin, A.E. Coumans, J.A.R. van Veen, J. Catal. 269 (2010) 201–218.

[26] R. Ryoo, J.M. Kim, C.H. Ko, C.H. Shin, J. Phys. Chem. C 100 (1996) 17718–17721.

[27] D. Zhao, C. Nie, Y. Zhou, S. Xia, L. Huang, Q. Li, Catal. Today 68 (2001) 11–20.

[28] C.S. Cundy, M.S. Henty, R.J. Plaisted, Zeolites 15 (1995) 342–352.

[29] M.H.F. Kox, E. Stavitski, J.C. Groen, J. Pérez-Ramírez, F. Kapteijn, B.M. Weckhuysen, Chem. Eur. J. 14 (2008) 1718–1725.

[30] E.J.M. Hensen, Q. Zhu, R.A.J. Janssen, P.C.M.M. Magusin, P.J. Kooyman, R.A. van Santen, J. Catal. 233 (2005) 123–135.

[31] E.J.M. Hensen, Q. Zhu, M.M.R.M. Hendrix, A.R. Overweg, P.J. Kooyman, M.V. Sychev, R.A. van Santen, J. Catal. 221 (2004) 560–574.

[32] S. Bordiga, R. Buzzoni, F. Geobaldo, C. Lamberti, E. Giamello, A. Zecchina, G. Leofanti, G. Petrini, G. Tozzola, G. Vlaic, J. Catal. 158 (1996) 486–501.

[33] F. Fan, K. Sun, Z. Feng, H. Xia, B. Han, Y. Lian, P. Ying, C. Li, Chem. Eur. J. 15 (2009) 3268–3276.

[34] K. Sun, F. Fan, H. Xia, Z. Feng, W.X. Li, C. Li, J. Phys. Chem. C 112 (2008) 16036–16041.

[35] F. Fan, Z. Feng, C. Li, Acc. Chem. Res. 43 (2009) 378–387.

[36] K.J. Sun, H. Xia, Z. Feng, R.A. van Santen, E.J.M. Hensen, C. Li, J. Catal. 254 (2008) 383–396.

[37] G.I. Panov, A.K. Uriarte, M.A. Rodkin, V.I. Sobolev, Catal. Today 41 (1998) 365–385.

[38] D. Meloni, R. Monaci, V. Solinas, G. Berlier, S. Bordiga, I. Rossetti, C. Oliva, L. Forni, J. Catal. 214 (2003) 169–178.

[39] S. GopaLakrishnan, A. Zampieri, W. Schwieger, J. Catal. 260 (2008) 193–197.

[40] R. Ravishankar, C.E.A. Kirschhock, P.-P. Knops-Gerrits, E.J.P. Feijen, P.J. Grobet, P. Vanoppen, F.C. De Schryver, G. Miehe, H. Fuess, B.J. Schoeman, P.A. Jacobs, J.A. Martens, J. Phys. Chem. B 103 (1999) 4960–4964.

[41] C.S. Cundy, P.A. Cox, Micropor. Mesopor. Mater. 82 (2005) 1–78.

[42] L.W. Beck, P. Lu, W.P. Weber, M.E. Davis, Micropor. Mesopor. Mater. 21 (1997) 361–368.

[43] P. Ratnasamy, R. Kumar, Catal. Today 9 (1991) 329–416.

[44] Y. Li, H. Xia, F. Fan, Z. Feng, R.A. van Santen, E.J.M. Hensen, C. Li, Chem. Commun. (2008) 774–776.